Check for updates

Geometric distortions in nickel (oxy)hydroxide electrocatalysts by redox inactive iron ions†

Rodney D. L. Smith, [ID] *[ab] Chiara Pasquini, [ID] [a] Stefan Loos, [ID] [ac] Petko Chernev, [ID] [a] Katharina Klingan, [ID] [a] Paul Kubella,[a] Mohammad Reza Mohammadi, [ID] [a] Diego González-Flores [ID] [a] and Holger Dau [ID] *[a]

The dramatic change in electrochemical behavior of nickel (oxy)hydroxide films upon incorporation of Fe ions provides an opportunity to establish effective electrocatalyst design principles. We characterize a photochemically deposited series of Fe–Ni (oxy)hydroxides by X-ray absorption spectroscopy and track the voltage- and composition-dependence of structural motifs. We observe a trigonal distortion in di-μ-hydroxo bridged Ni^{II}–Ni^{II} motifs that is preserved following a symmetric contraction of Ni–O bond lengths when oxidized to di-μ-oxo Ni^{IV}–Ni^{IV}. Incorporation of Fe ions into the structure generates di-μ-hydroxo Ni^{II}–Fe^{III} motifs in which Ni–Fe distances are dependent on nickel oxidation state, but Fe–O bond lengths are not. This asymmetry minimizes the trigonal distortion in di-μ-hydroxo Ni^{II}–Fe^{III} motifs and neighboring di-μ-hydroxo Ni^{II}–Ni^{II} sites in the reduced state, but exacerbates it in the oxidized state. We attribute both the Fe-induced anodic shift in nickel-based redox peaks and the improved ability to catalyze the oxygen evolution reaction to this inversion in geometric distortions. Spectroelectrochemical experiments reveal a previously unreported change in optical absorbance at *ca.* 1.5 V *vs.* RHE in Fe-containing samples. We attribute this feature to oxidation of nickel ions in di-μ-hydroxo Ni^{II}–Fe^{III} motifs, which we propose is the process relevant to catalytic oxygen evolution.

Broader context

Societal reliance on fossil fuels can be alleviated by the sustainable synthesis of chemical fuels by coupling electrochemical reactions to renewable energy technologies. A range of fuels and electrochemical reactions have been proposed, including H_2 generated from H_2O and hydrocarbons obtained from CO_2 reduction. The electrochemical synthesis of chemical fuels requires a complementary half-cell reaction to supply protons and electrons, regardless of fuel selection. To date, the oxidation of H_2O is the only such reaction that has received significant attention–maximizing its efficiency is thus a critical problem in the field. Nickel hydroxide undergoes dramatic changes in electrocatalytic performance upon incorporation of iron ions, transforming into one of the best known electrocatalysts for the oxygen evolution reaction. Here, we combine X-ray absorption spectroscopy and *in situ* spectroelectrochemistry to analyse the structure and electrochemical behaviour of a binary iron–nickel (oxy)hydroxide composition series. We identify iron-induced geometric distortions in the oxidized form of these materials. Correlation between electrochemical behaviour and the structural distortion leads us to propose that the energy penalties associated with these distortions are directly responsible for the changes in electrochemical behaviour. We propose that such an introduction of localized structural distortions can be applied to improve other electrocatalysts.

Introduction

The ability to efficiently drive the oxygen evolution reaction (OER) is key to processes such as the electrosynthesis of chemical fuels and electrocatalytic CO_2 reduction.[1,2] Decades of research on compositional tuning of solid state electrocatalysts for OER have yielded catalyst design principles focused on the manipulation of metal–oxygen bond strengths.[3–6] One of the most dramatic changes in OER performance arising from compositional tuning occurs upon incorporation of iron ions into nickel hydroxide, which shifts onset of OER cathodically by *ca.* 100 mV and improves catalyst response to overpotentials.[7–9] Similar, albeit less pronounced, changes exist upon incorporation of iron into cobalt oxyhydroxides.[10,11] These changes are well documented in the literature, but our fundamental understanding of them remains poor and the subject of intense debate. Determination of the structural changes underlying

[a] FB Physik, Freie Universität Berlin, Arnimallee 14, 14195 Berlin, Germany. E-mail: holger.dau@fu-berlin.de

[b] Department of Chemistry, University of Waterloo, 200 University Ave. W, Waterloo, ON, N2L 3G1, Canada. E-mail: rodsmith@uwaterloo.ca

[c] Fraunhofer Institute for Manufacturing Technology and Advanced Materials IFAM, Branch Lab Dresden, Winterbergstraße 28, 01277 Dresden, Germany

† Electronic supplementary information (ESI) available: Spectroelectrochemical CV and staircase voltammetry, XANES spectra, EXAFS spectra, bond length calibration plots, EXAFS fit parameters, bond angle calculations. See DOI: 10.1039/c8ee01063c

2476 | *Energy Environ. Sci.*, 2018, **11**, 2476–2485

This journal is © The Royal Society of Chemistry 2018

these performance changes may lead to effective catalyst design principles.

A central theme in modern research on Fe–Ni oxyhydroxides is the determination of the role that Fe ions play in OER. Recent studies have yielded structural and mechanistic information that is seemingly in conflict, resulting in numerous proposals and uncertainty over whether Fe plays a direct or indirect role in OER. While differences between fabrication protocols, testing conditions, and electrode handling protocols complicate direct comparisons between many of these studies, it is informative to summarize key structural characterizations and mechanistic proposals arising from them. In all reports, a pre-catalytic redox process is observed in Fe–Ni (oxy)hydroxides. This feature shifts anodically and decreases in size as Fe-content is increased.[9,12] This feature is universally assigned to oxidation of nickel ions, but is variably assigned to a 1-electron (i.e. a $Ni^{III/II}$ redox couple) or multi-electron process. The onset of electrocatalytic OER shifts cathodically upon incorporation of Fe, resulting in the convolution and eventual merger of the Ni-based pre-catalytic redox process with the electrocatalytic OER wave. Conflicting proposals, described below, have arisen in determining what physical or chemical changes occur within the material upon incorporation of iron to bring about these changes.

Arguments have been put forth that Fe-ions act as the catalytically active sites. This proposal was initiated by an X-ray absorption fine-structure spectroscopy (XAFS) study on a binary series of cathodically electrodeposited Fe–Ni (oxy)hydroxides.[13] The study showed that Fe ions experienced the same voltage-dependent structural changes as Ni ions within the material. Computational studies supported the authors' proposal that the observed contraction in Fe–O bond lengths would present a high-energy situation that enables Fe ions to act as catalytically active sites for OER. Characterization of Fe–Ni (oxy)hydroxide by Mössbauer spectroscopy had previously indicated that 21% of Fe ions were oxidized from Fe^{III} to Fe^{IV} during electrocatalytic operation;[14] the persistence of Fe^{IV} sites even after the applied voltage was removed led to the conclusion that the Fe^{IV} sites were not catalytically competent, but would be expected to influence the structure and behaviour of the materials. A spectroelectro-chemical study on Fe–Ni (oxy)hydroxide prepared by pH precipitation of a $3Ni^{II}:1Fe^{III}$ solutions exhibited a complete merger of the pre-catalytic redox process with the catalytic wave.[15] A combined computational study supported the oxidation of Fe^{III} to Fe^{IV} at the onset of electrocatalytic OER. Most recently, a study on an Fe–Ni (oxy)hydroxide material fabricated by pulsed laser ablation included the proposal that a penta-coordinated Fe^{VI} species forms at terminal sites and is likely responsible for OER.[16] The proposal was supported by Mössbauer spectroscopy and vibrational spectroelectrochemistry in organic electrolyte solutions.

Arguments have also been put forth for a nickel-based active site, where Fe ions play an indirect role. A systematic analysis on hydrothermally synthesized Fe–Ni (oxy)hydroxides by XAFS and in operando XAS concluded that iron ions remain in an Fe^{III} state.[12] The average oxidation state of nickel ions was observed to decrease under catalytic operation for films with >30 atomic

percent Fe, which the authors attribute to an inability to accumulate oxidized nickel sites due to facile OER kinetics. A decrease in size of the pre-catalytic redox process is generally observed in Fe–Ni (oxy)hydroxides and is typically interpreted as stabilization of Ni sites in lower oxidation states by Fe^{III}. An analysis of anodically electrodeposited Fe–Ni (oxy)hydroxides by electrochemical techniques and X-ray absorption near-edge spectroscopy (XANES), however, indicated the opposite.[17] The average oxidation state of nickel ions in the oxidized phase increased from ca. 3.2 to 3.6 as the Fe content was increased from 0 to 10 molar percent. The authors concluded that the high Lewis acidity of Fe^{III} promotes oxidation of Ni^{II} to Ni^{IV}, thereby facilitating catalysis.

Herein, we identify the structural motifs present in a series of photochemically deposited Fe–Ni (oxy)hydroxide materials using quasi in situ XAFS and track their dependence on voltage and composition. We identify a previously unreported change in optical absorbance properties in Fe-containing compositions by spectroelectrochemical measurements and analyse trends between spectroelectrochemical behaviour parameters and structural motifs to assign electrochemical processes. We propose that the changes in electrochemical behaviour of these materials originate from the exacerbation of geometric distortion in the coordination environment of nickel ions by incorporation of redox-inactive Fe^{III} ions.

Experimental

Materials

Nickel(II) 2-ethylhexanoate (78% in 2-ethylhexanoic acid, Strem Chemicals Inc.) and iron(III) 2-ethylhexanoate (6% solution in mineral spirits, Strem Chemicals Inc.) were used as received. Fluorine-doped tin oxide coated glass (FTO; TEC-7 grade, Solems S.A.) was cleaned immediately before use by sequential ultrasonication in detergent solution, MilliQ H_2O, then isopropanol. The FTO was then dried under a stream of N_2 and placed under UV lamp (Dinies UV Chamber M1) for 15 minutes. Electrolyte solutions were prepared by dissolving potassium hydroxide (>85%, Carl Roth) in MilliQ H_2O (18.2 MΩ) and aging the solution over $Ni(OH)_2$ to remove Fe impurities from the solution, as previously described.[8]

Fabrication

A series of metal oxide films based on the formula $Fe_{100-y}Ni_yO_x$ were fabricated on FTO by photochemically induced decomposition of metal–organic precursors.[18,19] Precursor solutions were prepared by dissolving the appropriate stoichiometric ratios of Fe(III) 2-ethylhexanoate and Ni(II) 2-ethylhexanoate in ethanol to achieve a total metal ion concentration of 0.3 M. Aliquots of these solutions were dropped onto FTO substrates being rotated at 3000 rpm and spun for 1 minute. Irradiation of the resultant solid-state precursor films with UV light (1000 min) yielded the desired metal oxide films. Metal oxide films are labelled herein by the molar proportion of nickel in the precursor solutions (i.e., 100% Ni, 88%, etc.). Scanning electron microscopy

has previously shown that the addition of Fe decreases the apparent surface roughness of photochemically deposited nickel hydroxide.[18,19]

Electrochemical and spectroelectrochemical measurements

Electrochemical measurements were performed using a Bio-Logic SP-300 potentiostat. All experiments were performed in a single-compartment polyethylene cell using purified 1 M KOH as the electrolyte solution, a Pt counter electrode and a Gaskatel® Hydroflex RHE reference electrode (Gaskatel GmbH; Germany). A quartz cuvette served as the reaction cell for spectroelectro-chemical measurements and a polyethylene cell was employed to prepare samples for X-ray absorption spectroscopy (XAS). Cyclic voltammetry experiments were performed between 1.0 and 1.7 V *vs.* RHE at a scan rate of 1 mV s^{-1}. Steady state currents for electrokinetic analysis were determined by staircase voltammetry with the steady-state current and absorbance values taken at the end of the 60 s, 10 mV steps; data was recorded twice in both anodic and cathodic scan directions. All current densities are reported with respect to geometric surface area of the electrodes. Cell resistances were *ca.* 10 Ω for all experiments, as measured by impedance spectroscopy before experiments. Experiments were carried out without resistance compensation; data was numerically corrected for uncompensated resistance before analysis of electrokinetics (*i.e.* only Tafel plots are numerically corrected).

Spectroelectrochemical data was recorded for compositions between 50% and 100% Ni with 430 nm light using an in-house setup that was previously described.[20] Higher Fe-contents were not examined due to the known decrease in catalytic OER performance.[12,13] The intensity of transmitted light was recorded for the as-prepared sample in a fully assembled cell and compared with the transmittance during experiments to track changes in absorbance relative to the as-prepared films ($\Delta A_{430\,nm}$).[20]

X-ray absorption spectroscopy

Samples were prepared for quasi *in situ* XAS experiments by applying the desired voltage protocol then submerging the electrode in liquid nitrogen. Films examined here were prepared by five different protocols: (i) no exposure to electrolyte solution (as-prepared samples), (ii) application of 1.5 V (oxidized films), (iii) application of 1.7 V (catalytic samples), (iv) sequential application of 1.7 V then 0.9 V (reduced samples), and (v) sequential application of 1.7 V, 0.9 V, then 1.5 V (re-oxidized samples). All voltage steps were 10 min. in length. All five protocols were examined for compositions between 100% Ni and 62% Ni. Owing to the absence of a well-resolved oxidation peak, 50% Ni, 38% Ni and 25% Ni were only examined in the as-prepared, catalytically active and electrochemically reduced states.

XAS was performed at the KMC-3 beamline at the BESSY II synchrotron facility in Berlin, Germany. The incident X-ray energy was scanned through the Fe and Ni K-edge regions using a silicon(111) double-crystal monochromator. Measurements were performed at 20 K with samples positioned with a grazing-angle geometry in a liquid helium cooled cryostat. High purity metal foils positioned behind the sample served as calibration standards (10 μm Fe or Ni foils, >99.99% purity, Goodfellow Cambridge Limited) and fluorescence signals were recorded at a 13-element windowless Ge detector (Ultra-LEGe detector, Canberra) positioned perpendicular to the incident beam.

X-ray absorption fine-structure spectroscopy simulations

The spectral data for the Fe and Ni K-edges was processed and simulated using in-house software packages. Coordination shells are defined to consist of a number of atoms of a given element (N_i) positioned at a given distance (R_i) from the absorbing atom. Both N_i and R_i represent average values within the material, with variations in R_i captured by the Debye–Waller parameter (σ_i). The sum of oscillations for all coordination shells are dampened by an amplitude reduction factor (S_o^2). The scattering amplitude ($A(R_i,k)_i$) and phase correction (ϕ_i) parameters for each shell were obtained by *ab initio* calculations using FEFF 8.4.[21]

Two simulation strategies were performed to gain quantitative insights into the Fe and Ni coordination environments. A minimal fit model was developed to obtain σ_{M-O} and σ_{M-M} values for the Fe and Ni environments. Under the assumption that all metal centres are octahedrally coordinated, N_{M-O} values in each sample were fixed at 6. Bond distances (R_i) and Debye–Waller factors (σ_i) were then mathematically fitted. For cases where multiple M–O shells were required, both N_{M-O} values were fitted with the restriction that their sum equals 6. A refined simulation approach was then performed by defining two distinct M–M shells with σ_{M-M} values of 0.066 Å in all samples, in line with values previously utilized in nickel (oxy)hydroxide systems.[12,13,22,23] A single σ_{Ni-O} value was group-fitted for all Ni–O shells for samples with the same voltage protocol; all R_i values were fitted independently. Simulations were performed on k^3 weighted data in the k-range 3–12 Å^{-1} for Fe and 3–14 Å^{-1} for Ni. Errors were estimated as previously described, with a useful R-space range defined between 1.0–3.5 Å.[22]

Results & discussion

Electron transfer dynamics

Spectroelectrochemical cyclic voltammetry (CV) experiments on samples between 100% Ni and 50% Ni contain an anodic peak, $E_{p,a}$, and a corresponding cathodic peak, $E_{p,c}$, (Fig. 1A). A cathodic shift in $E_{p,a}$ occurs between the first and second CV cycles, as previously reported,[24,25] after which stable behaviour is observed. A separation of *ca.* 100 mV exists between $E_{p,a}$ and $E_{p,c}$ in all samples and both features experience an anodic shift as the Fe-content of the material increases. A simultaneous cathodic shift in the catalytic OER wave results in convolution of the two features, with the eventual disappearance of $E_{p,a}$ at a composition of 50% Ni. The 2nd derivative of current density with respect to potential (d^2j/dE^2) facilitates tracking of $E_{p,a}$ as the first positive peak for $E_{p,a}$ persists even after convolution of

2478 | *Energy Environ. Sci.*, 2018, **11**, 2476–2485

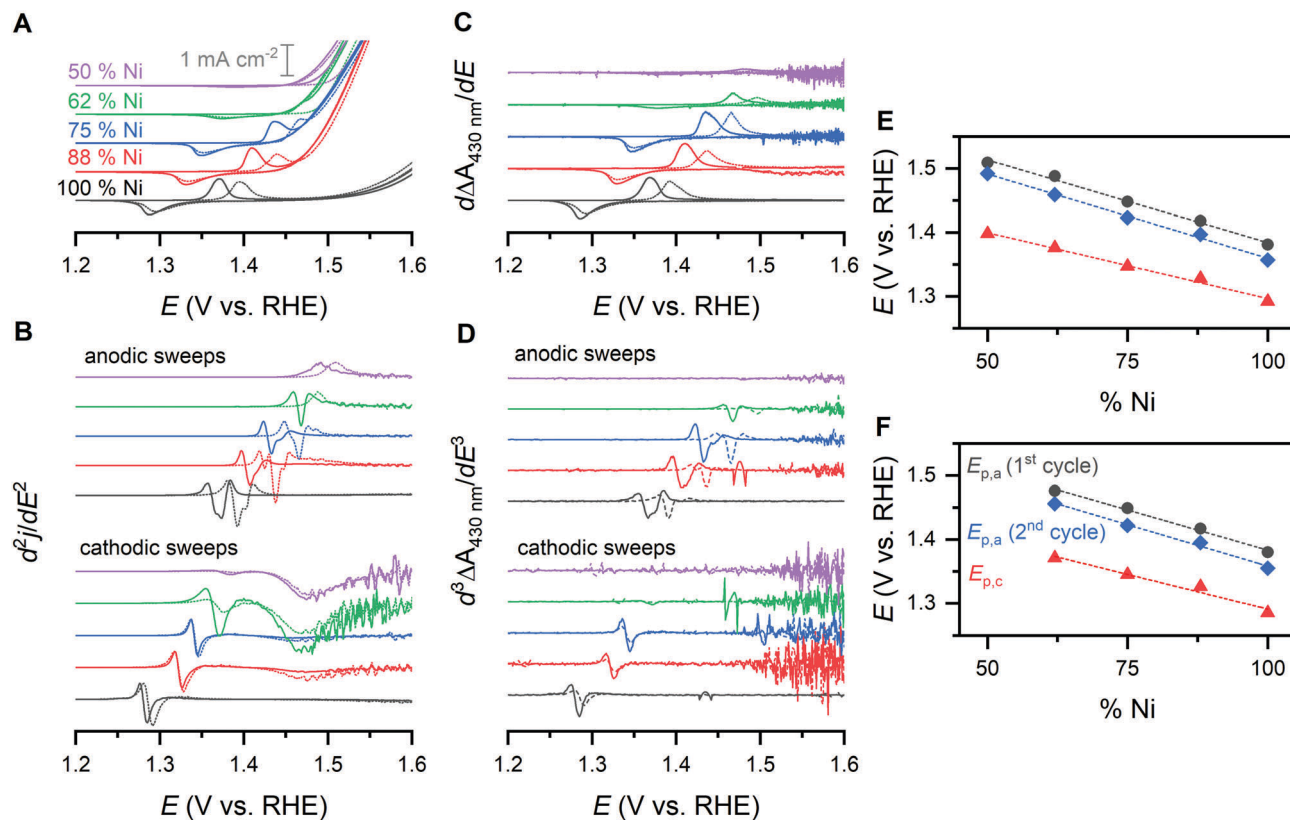This journal is © The Royal Society of Chemistry 2018

Fig. 1 Spectroelectrochemical behaviour of the Fe−Ni (oxy)hydroxide composition series. (A) Cyclic voltammograms recorded at 1 mV s^{-1} in 1 M KOH and (B) the second derivative of the data. (C) The first derivative and (D) third derivative of $\Delta A_{430\,nm}$. In all panels the samples shown are 100% Ni, 88% Ni, 75% Ni, 62% Ni and 50% Ni, listed from bottom to top. The dashed lines represent the first voltammetric cycle and the solid lines the second cycle. Location of $E_{p,a}$ (first cycle black circles; steady state blue diamonds) and $E_{p,c}$ (red triangles) as determined from (E) the electrochemical data and (F) the spectroscopic data.

$E_{p,a}$ with the catalytic wave (Fig. 1B). Plotting this feature as a function of composition reveals a linear anodic shift with a rate of 2.6 mV%$_{Fe}$$^{-1}$ that continues after merging with the catalytic wave (Fig. 1E). Similar analysis of the cathodic sweep segments, in which $E_{p,c}$ is visible for all compositions, indicates a linear shift of 2.1 mV%$_{Fe}$$^{-1}$ for $E_{p,c}$. These derivative plots reveal asymmetric character in $E_{p,a}$ between 100% Ni and 75% Ni that suggests overlapping redox processes; $E_{p,c}$ exhibits a gradual onset, but no clear sign of overlapping processes is present. This behaviour is in general agreement with previous reports for iron–nickel (oxy)hydroxide materials,[7,9,12,26] excepting differences in the composition at which $E_{p,a}$ merges with the catalytic wave. This merger was reported at 59% Ni for cathodically electro-deposited films[9] and at 45% Ni for hydrothermally prepared Fe–Ni (oxy)hydroxide.[12]

Changes in $\Delta A_{430\,nm}$ during CV experiments corroborate the electrochemical measurements. The validity of Beer's law for nickel hydroxide films has been previously confirmed.[27] The derivative of $\Delta A_{430\,nm}$ with respect to voltage thus yields a rate of change for chemical species within the film, which can be qualitatively compared to current density (Fig. 1C).[28,29] Analysis of this data reveals the same behaviour as the electrochemical data: an asymmetric anodic redox process, anodic shifting of $E_{p,a}$ and $E_{p,c}$ at a rate of *ca.* 2 mV%$_{Fe}$$^{-1}$, and continued shift

after the redox process merges into the catalytic wave. A sample of resistance-corrected data is provided in Fig. S1 (ESI†).

Electrocatalysis of the oxygen evolution reaction

Catalytic performance parameters extracted from the composition series show an abrupt change upon incorporation of small amounts of iron, followed by a gradual change with further additions. The onset of catalysis (E_{OER}), defined here as the onset of linearity in log(j) *vs.* E plots (Fig. 2), jumps from 1.471 V for 100% Ni to 1.396 V for 88% Ni before gradually trending anodically to 1.426 V in 50% Ni. The Tafel slope jumps from 72 mV dec^{-1} in 100% Ni to 33 mV dec^{-1} in 88% Ni, then trends to 28 mV dec^{-1} in 50% Ni. A relatively high 1.612 V is required for 100% Ni to reach 1 mA cm^{-2} and 1.684 V for 10 mA cm^{-2} (extrapolated value). These values are significantly lowered for 88% Ni (1.480 V and 1.514 V) and 75% Ni (1.471 V and 1.502 V), before gradually trending anodically. Experiments were performed to 1.7 V *vs.* RHE without resistance compensation (Fig. S2, ESI†). When corrected for uncompensated resistance all plots exhibit linearity from E_{OER} until the highest voltage examined (Fig. 2).

Changes in optical properties during acquisition of electro-kinetic data reveal a transition that has not been previously reported. The $\Delta A_{430\,nm}$ values recorded during staircase voltam-metry experiments show the well-known electrochromic behaviour

This journal is © The Royal Society of Chemistry 2018

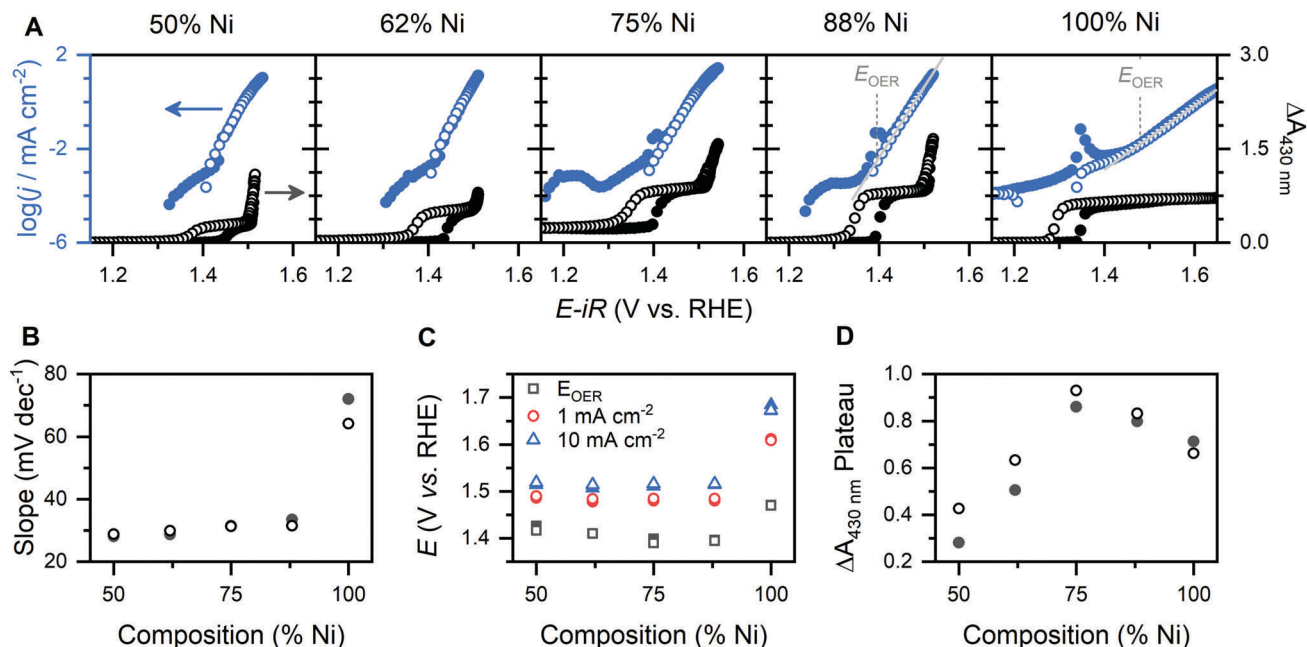*Energy Environ. Sci.,* 2018, **11**, 2476–2485 | **2479**

Fig. 2 Electron transfer kinetics were measured for the Fe−Ni (oxy)hydroxide series while simultaneously tracking absorbance of 430 nm light. (A) Steady state current density and change in absorbance relative to the as-prepared films ($\Delta A_{430\,nm}$) were recorded in the anodic (solid data points) and cathodic (hollow data points) directions by staircase voltammetry. Comparison of (B) Tafel slope, (C) voltages for onset of linearity in Tafel plots (E_{OER}) and voltages where 1 and 10 mA cm^{-2} are attained, and (D) the height of the $\Delta A_{430\,nm}$ plateau as a function of catalyst composition. The staircase voltammetry experiments were performed twice for each film; the solid data points in panels (B)−(D) represent the values from the first series and the hollow points the second series.

of nickel hydroxide, with $\Delta A_{430\,nm}$ increasing at $E_{p,a}$ in all samples and decreasing at $E_{p,c}$. For 100% Ni a plateau in $\Delta A_{430\,nm}$ continues throughout the anodic and cathodic scan directions, only changing when $E_{p,c}$ is reached. All Fe-containing samples exhibit a second, fully reversible increase in $\Delta A_{430\,nm}$ at *ca.* 1.5 V. This increase is distinct from the noise due to bubble formation (Fig. S2, ESI†). The height of the $\Delta A_{430\,nm}$ plateau following the change increases linearly with Fe-addition up to 75% Ni, then decreases linearly with further Fe-addition (Fig. 2D); these trends are maintained even after normalizing for nickel content.

X-ray absorption near-edge spectroscopy

The near-edge spectra of the quasi *in situ* XAS spectra confirm that $E_{p,a}$ and $E_{p,c}$ are Ni-based and multi-electron in nature (Fig. 3 and Fig. S3, ESI†). Both the Ni K-edge and pre-edge shift to higher energies for the oxidized, catalytic and re-oxidized samples than for the as-prepared and reduced samples. The K-edge for octahedral nickel ions shifts linearly at a rate of 1.55 eV per oxidation state change,[12,30] and the pre-edge at 0.6 eV per oxidation state change.[30] Normalization of the shift of these spectral features relative to the as-prepared sample (ΔE_{edge}, $\Delta E_{pre-edge}$) thus yields an estimate of oxidation state change relative to the as-prepared films for each composition (Fig. 3C and Fig. S4, ESI†). Comparison of the different voltage protocols reveals that Ni sites in the films are partially oxidized in all as-prepared samples, and that $E_{p,a}$ and $E_{p,c}$ induce an oxidation state change of 1.8–2.0 units in 100% Ni. The slight decrease in average nickel oxidation state observed during active OER catalysis has been previously attributed to an

increased rate of hole transfer from metal centers to oxygen ligands during OER.[12] The reversible change in nickel oxidation state due to $E_{p,a}$ and $E_{p,c}$ can be taken as the difference between reduced and re-oxidized films. This value decreases as Fe is incorporated, but changes of > 1.0 oxidation state are observed until 50% Ni. At 50% Ni $E_{p,a}$ can no longer be resolved from the electrocatalytic wave and an oxidation state change of 0.3 units is observed between catalytic and reduced samples. Average nickel oxidation states above 3.0 in both the oxidized and catalytic samples necessitates the assignment of $E_{p,a}$ and $E_{p,c}$ to a Ni$^{IV/II}$ redox transition.

The Fe K-edge location is insensitive to voltage in all compositions examined (Fig. 3B and Fig. S5, ESI†). Crystalline standards indicate a 4.6 eV shift in K-edge per oxidation state change for Fe ions.[20] The average K-edge location, determined by the integral method,[31] for all as-prepared and reduced samples (7125.7 ± 0.4 eV) and oxidized, catalytic and re-oxidized samples (7125.5 ± 0.4 eV) are indistinguishable from one another, indicating exclusive Fe(III) for all conditions.

Extended X-ray absorption fine-structure spectroscopy

Qualitative comparison of EXAFS data acquired from the Fe and Ni K-edges reveals differences in the voltage-dependent structural environments for the two elements. The Fe and Ni environments are similar across the composition series in that they present features characteristic of di-μ-oxo/hydroxo-bridged metal ions in the Fourier-transformed data: M–O distances between *ca.* 1.8–2.1 Å and M–M distances between 2.8–3.1 Å (Fig. 4).[12,13,22,23,32,33] For simplicity we will refer to these M–M distances as di-μ-oxo bridged

2480 | *Energy Environ. Sci.*, 2018, **11**, 2476–2485

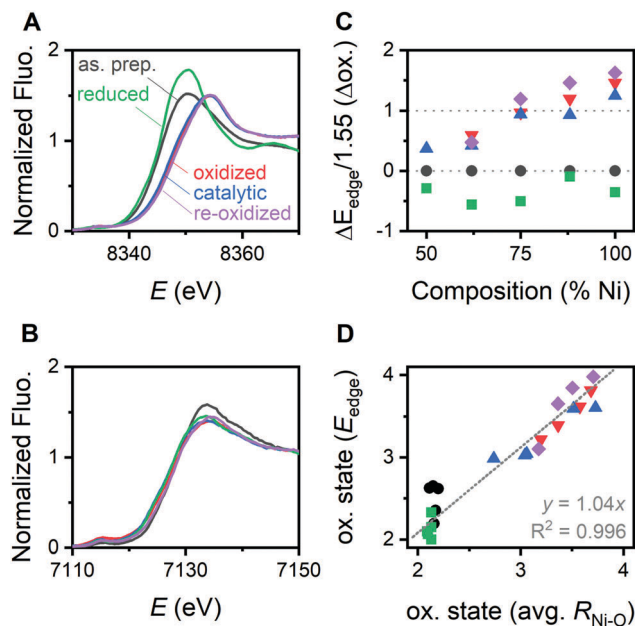This journal is © The Royal Society of Chemistry 2018

Fig. 3 Voltage-dependent X-ray absorption near-edge spectra and oxidation state changes. Spectra for the (A) Ni K-edge of 100% Ni, and (B) the Fe K-edge region of 88% Ni. (C) Normalized relative shifts in the Ni K-edge for the composition series giving the oxidation state change, relative to the as-prepared sample for each composition. (D) Comparison of Ni oxidation state as determined by XANES and the length of weighted-average Ni–O bond lengths. Absolute oxidation states were calculated for E_{edge} by defining the lowest K-edge position as Ni^{2+}, and for R_{Ni-O} by calibration against literature values (Fig. S8, ESI†). All panels contain data for as-prepared (black), oxidized (red), catalytic (blue), reduced (green) and re-oxidized (purple) films.
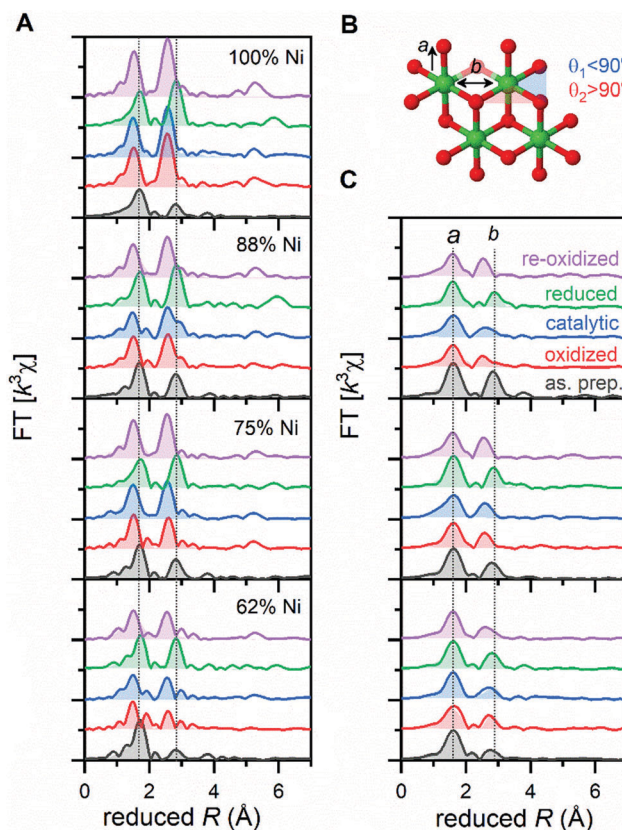

Fig. 4 Fourier-transformed X-ray absorption fine-structure spectra at the (A) Ni K-edge and (C) Fe K-edge. (B) Schematic detailing distances observed in the spectra and highlighting bond angle differences due to a trigonal distortion. Panels contain data for as-prepared (black), oxidized (red), catalytic (blue), reduced (green) and re-oxidized (purple) films. Solid lines are experimental data and shading is the EXAFS simulations.

motifs, with the understanding that hydroxide bridges exist in the reduced phase and oxide bridges in the oxidized phase. In the Ni environment the catalytic, oxidized and re-oxidized samples all present shorter distances for both structural features than as-prepared and reduced samples. This is easily understood as a uniform shortening of Ni–O bond lengths upon oxidation of Ni^{II} to Ni^{IV} that induces contraction of the di-μ-oxo-bridged Ni–M motifs, where M is either Ni or Fe. The Fe environment exhibits different behaviour. The peak corresponding to di-μ-oxo-bridged Fe–M motifs qualitatively tracks that in the Ni dataset, with shorter distances observed for oxidized, catalytic and re-oxidized samples than for as-prepared and reduced samples. The Fe–O feature, however, remains static for all conditions. The shortening of Ni–O bonds upon electrochemical oxidation thus decreases the average Fe–M distance but has a negligible impact on Fe–O distances. As-prepared films exhibit significant dispersion in bond distances relative to all other films, as evidenced by the low intensity of the Fourier-transformed EXAFS peaks. An increase in short-range ordering is observed following electrochemical use, though the lack of a feature at twice the M–M distance in all but 100% Ni and 88% Ni indicate that this ordering is limited to distances under 4 Å (Fig. S6, ESI†).

Minimal-fit simulation model

The 100% Ni sample is successfully described using two shells for all voltage protocols: R_{Ni-O} decreases from 2.045 Å in reduced

films to 1.878 Å in oxidized films, with a concurrent decrease in R_{Ni-Ni} from 3.085 to 2.833 Å. Bond distances and Debye–Waller factors are in agreement with values previously reported for nickel hydroxide films (Table S1, ESI†);[12,13,22,23,32,33] reasonable coordination numbers were obtained for all voltage conditions when mathematically fitted.

The minimal fit approach requires a single M–O shell and a single M–M shell, for both the Ni and Fe K-edges, for all compositions in the as-prepared and reduced states (Tables S1 and S2, ESI†). The R_{Ni-M} values become smaller and σ_{Ni-M} values (standard deviation in bond lengths) become larger as the Fe-content increases, while R_{Ni-O} and σ_{Ni-O} remain constant across the composition series. In contrast, the oxygen coordination sphere around Fe ions becomes more ordered as Ni content increases: R_{Fe-O} values increase with a concurrent decrease in σ_{Fe-O} as Ni content increases. Blending Fe into photochemically deposited nickel (oxy)hydroxide appears to impose greater ordering on Fe sites. Throughout the composition series R_{Fe-O} remains shorter than R_{Ni-O} in the reduced phase, but longer in the oxidized phase. The R_{M-M} values for 100% Ni and 0% Ni were 3.085 and 3.029 Å, respectively. Both R_{Ni-M} and R_{Fe-M} were found to trend from these native values towards that for the opposing element. A linear relationship between R_{Fe-M} and Fe-content for compositions

between 38% Ni and 88% Ni (Tables S1 and S2; Fig. S10, ESI†) suggests that Fe is uniformly incorporated across that composition range, with possible phase segregation appearing at higher Fe concentrations. The extent of Fe-incorporation prior to phase segregation is larger than that reported for electrodeposited Fe–Ni (oxy)hydroxides,[13] but similar to that recently observed in photo-chemically deposited Fe–Co oxides.[20] The trends in the minimal fit model, combined with large $\sigma_{M–M}$ values that grow with successive Fe incorporation, indicate that multiple M–M distances are present in the composition series.

Refined simulation model

The presence of a distinct Ni–Fe vector is implied by a steady increase in Debye–Waller factors ($\sigma_{M–M}$) as Fe-content increases for the minimal fit model (Tables S1 and S2, ESI†). We therefore split the Ni–M feature into two shells, representative of di-μ-oxo bridged Ni–Ni and di-μ-oxo bridged Ni–M motifs, to acquire refined structural insights (Table 1 and Table S3; Fig. S7, ESI†). The as-prepared and the electrochemically reduced films are successfully described by a single $R_{Ni–O}$ with an average value of 2.056 Å over the composition series. The two Ni–M coordination shells yield $R_{Ni–M}$ values centred at 2.98 and 3.10 Å in the as-prepared films, and 2.95 and 3.09 Å in the electrochemically reduced films. No clear composition-dependent trends are observed for either $N_{Ni–M}$ value in as-prepared samples, likely owing to their extreme disorder. The electrochemically reduced films, however, show a clear trend: $N_{Ni–M}$ values for the shorter Ni–M distance increase as Fe content increases, while $N_{Ni–M}$ for the longer Ni–M distance decreases (Fig. 5). The shorter distance in the reduced phase is thus assigned to di-μ-oxo bridged Ni–Fe sites and the longer distance to di-μ-oxo bridged Ni–Ni sites.

The Ni–O feature splits into two peaks with average distances of 1.884 ($R_{Ni–O1}$) and 2.056 Å ($R_{Ni–O2}$) upon oxidation. The stability of $R_{Ni–O1}$ and $R_{Ni–O2}$ across the composition series supports the assignment of only two Ni oxidation states in these materials. The coordination numbers for these shells vary linearly with Fe content, with $N_{Ni–O1}$ decreasing and $N_{Ni–O2}$ increasing as Fe content increases (Fig. 5A). The length of Ni–O bonds has been
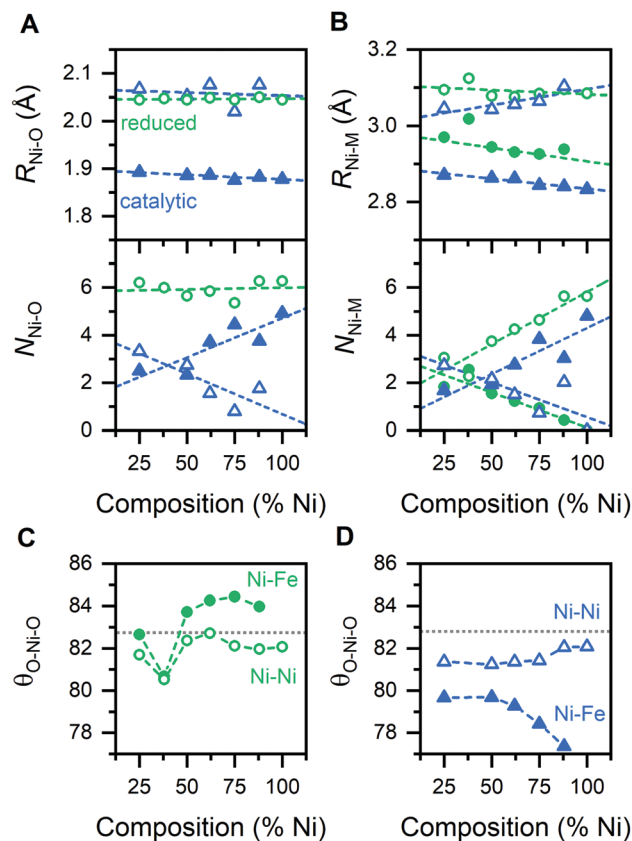

Fig. 5 Composition-dependent trends in bond length and coordination number for (A) Ni–O and (B) Ni–M bonds in catalytic samples (blue) and reduced samples (green). Composition-dependent O–Ni–O bond angles in the di-μ-oxo bridged motif in the (C) reduced and (D) catalytic samples. Angles for di-μ-oxo bridged Ni–Fe motifs are represented by solid data points and di-μ-oxo bridged Ni–Ni by hollow data points. Horizontal grey lines in panels (C) and (D) mark the bond angle observed in β-Ni(OH)$_2$. Trend lines are drawn in all panels to guide the eye.

shown to correlate to nickel oxidation state and the values for $R_{Ni–O1}$ and $R_{Ni–O2}$ support their assignment to Ni^{IV} and Ni^{II}, respectively (Fig. S8, ESI†).[12] The weighted average Ni–O bond length for each sample yields average nickel oxidation state values that are

Table 1 EXAFS simulation parameters for the Ni K-edge of catalytic and reduced samples from the Fe–Ni (oxy)hydroxide series[a]

% Ni	$N_{Ni–O1}$	$R_{Ni–O1}$ (Å)	$N_{Ni–O2}$	$R_{Ni–O2}$ (Å)	$N_{Ni–M1}$	$R_{Ni–M1}$ (Å)	$N_{Ni–M2}$	$R_{Ni–M2}$ (Å)	R_{f}
100[b]	4.9 (0.3)	1.878 (0.004)			4.8 (0.2)	2.833 (0.002)			15.0
88[b]	3.8 (0.4)	1.883 (0.007)	1.8 (0.4)	2.076 (0.020)	3.0 (0.3)	2.841 (0.005)	2.0 (0.3)	3.103 (0.008)	9.1
75[b]	4.5 (0.6)	1.876 (0.010)	0.8 (0.5)	2.020 (0.062)	3.8 (0.3)	2.844 (0.004)	0.7 (0.4)	3.065 (0.023)	13.7
62[b]	3.7 (0.4)	1.887 (0.008)	1.6 (0.4)	2.076 (0.023)	2.8 (0.3)	2.862 (0.006)	1.5 (0.4)	3.057 (0.012)	14.9
50[b]	2.3 (0.3)	1.886 (0.012)	2.7 (0.4)	2.053 (0.012)	1.9 (0.3)	2.863 (0.008)	2.2 (0.3)	3.043 (0.008)	27.3
25[b]	2.5 (0.3)	1.893 (0.012)	3.3 (0.3)	2.067 (0.011)	1.7 (0.3)	2.871 (0.012)	2.7 (0.3)	3.046 (0.008)	15.8
100[c]			6.3 (0.3)	2.045 (0.004)			5.6 (0.2)	3.085 (0.002)	9.4
88[c]			6.3 (0.4)	2.050 (0.003)	0.4 (0.4)	2.938 (0.054)	5.6 (0.4)	3.095 (0.005)	9.0
75[c]			5.4 (0.4)	2.045 (0.005)	0.9 (0.4)	2.926 (0.024)	4.6 (0.4)	3.084 (0.005)	13.0
62[c]			5.9 (0.4)	2.049 (0.005)	1.2 (0.4)	2.931 (0.021)	4.3 (0.4)	3.076 (0.007)	16.3
50[c]			5.7 (0.4)	2.045 (0.005)	1.6 (0.4)	2.944 (0.019)	3.7 (0.4)	3.078 (0.009)	15.0
38[c]			6.0 (0.3)	2.047 (0.004)	2.6 (0.6)	3.018 (0.017)	2.3 (0.6)	3.124 (0.021)	18.4
25[c]			6.2 (0.3)	2.045 (0.004)	1.8 (0.4)	2.970 (0.016)	3.1 (0.4)	3.094 (0.011)	20.8

[a] S_0^2 = 0.9; brackets represent error in values. [b] Catalytic samples (1.7 V vs. RHE; $\sigma_{Ni–O}$ = 0.070 ± 0.004 Å; $\sigma_{Ni–M}$ = 0.066 Å. [c] Reduced samples (1.7 then 0.9 V vs. RHE); $\sigma_{Ni–O}$ = 0.072 ± 0.002 Å; $\sigma_{Ni–M}$ = 0.066 Å.

Table 2   Geometric parameters of observed structural motifs

Structural motif	R^a (Å)	$\theta_{O-Ni-O}{}^b$ (°)	$\theta_{O-Fe-O}{}^b$ (°)
$Ni^{II}-O$	2.056 ± 0.019		
$Ni^{IV}-O$	1.884 ± 0.005		
$Fe^{III}-O$	1.966 ± 0.025		
Di-μ-oxo $Ni^{II}-Ni^{II}$	3.091 ± 0.016	82.5	
Di-μ-oxo $Ni^{IV}-Ni^{IV}$	2.850 ± 0.016	81.7	
Di-μ-oxo $Ni^{II}-Fe^{III}$	2.955 ± 0.035	83.1	87.8
Di-μ-oxo $Ni^{II}-Fe^{III}{}^c$	3.071 ± 0.022	78.3	82.6

^{a} Average from all oxidized or reduced samples; error represents standard deviation. ^{b} Geometric calculations described in ESI. ^{c} Value for oxidized films.

in agreement with the average oxidation state measured by XANES (Fig. 3D). The composition-dependent behaviour of the Ni–O coordination shell supports the conclusions that the average Ni oxidation state is representative of a mixture of Ni^{II} and Ni^{IV} sites, and that Fe incorporation stabilizes a portion of the film in the Ni^{II} state.

The di-μ-oxo Ni–M shells continue to show composition-dependent variation in R_{Ni-M} upon oxidation but contract to become centred at *ca.* 2.850 and 3.071 Å (Fig. 5B). An inversion of Fe-dependent trends in N_{Ni-M} values occurs in oxidized phases: N_{Ni-M} values for the shorter Ni–M distance decrease with addition of Fe, while N_{Ni-M} for the longer distance increases (Fig. 5B). The longer Ni–M distance in the oxidized phases is thus assigned to di-μ-oxo bridged Ni–Fe sites. The inversion of relative Ni–M distances when transitioning from reduced to oxidized states is attributed to the insensitivity of R_{Fe-O} to the oxidation state of the Ni ions, and its location between R_{Ni-O1} and R_{Ni-O2} (1.966 Å *vs.* 1.884 and 2.056 Å).

Peaks attributable to di-μ-oxo bridged Fe–M motifs in the FT EXAFS of the Fe K-edge data are significantly lower in intensity than those for the Ni K-edge data, signifying a greater degree of disorder in the Fe environment. It is clear that the EXAFS feature shifts upon oxidation of nickel ions (Fig. 4C) and weak trends can be identified in the simulation parameters. Confident analysis of trends in the Fe data as was done for the Ni environment is inhibited by low N_{Fe-M} values with large potential errors (Table S4, ESI†). Despite the disorder in the Fe–M coordination shell it is notable that R_{Fe-O} is a constant 1.966 ± 0.025 Å through all compositions and voltage protocols (Table S2, ESI†).

Trends in the composition- and voltage-dependency of structural motifs enable assignment of four distinct Ni–M distances observed across the series to specific structural motifs within the series (Table 2).

Discussion

The structure of disordered nickel (oxy)hydroxide and the iron-substituted analogues is often compared to layered double-hydroxide phases. These phases consist of metal ions coordinated to six hydroxide (or oxide) ligands, with neighbouring cations bound together through di-μ-oxo bridges to yield 2-dimensional sheets. Rather than octahedral symmetry about the transition metal ion, layered double hydroxide phases exhibit a trigonal distortion that imparts D_{3d} symmetry on the metal centers.[34] This distortion is

accomplished without disrupting M–O distances by formation of two distinct O–M–O bond angles (θ_{O-Ni-O}): in the mineral theophrasite R_{Ni-O} are uniformly 2.08 Å while θ_{O-Ni-O} values of 82.8° and 97.2° are observed, with the shorter angle oriented between di-μ-oxo bridged nickel sites as depicted in Fig. 4B.[34] Geometric analysis of R_{Ni-O} and R_{Ni-Ni} values obtained here indicate a θ_{O-Ni-O} angle of 82.5° and 81.7° for the reduced and oxidized forms of 100% Ni, respectively, suggesting that a trigonal distortion is present (Table 2).

Tracking θ_{O-Ni-O} values as a function of voltage and composition reveals that Fe ions influence the trigonal distortion at nickel sites differently in the oxidized and reduced phases. The incorporation of Fe splits di-μ-oxo bridged Ni–Ni structural motifs into Ni–Ni and Ni–Fe motifs; the difference between R_{Fe-O} and R_{Ni-O} introduces asymmetry that disrupts the distortion of di-μ-oxo bridged Ni–Fe motifs (Table 2). In the electrochemically reduced phase this asymmetry increases θ_{O-Ni-O} and θ_{O-Fe-O} values towards those expected for undistorted octahedra, which would stabilize the material by relieving geometric strain. The significant change in R_{Ni-O} upon oxidation of Ni^{II} to Ni^{IV} induces the opposite effect, decreasing θ_{O-Ni-O} to an average of 78.3° and θ_{O-Fe-O} to an average of 82.6°. This increased geometric strain effectively destabilizes the oxidized phase, posing a thermodynamic penalty to oxidation. Individual θ_{O-Ni-O} values calculated for di-μ-oxo Ni–Ni and di-μ-oxo Ni–Fe motifs in the oxidized and catalytically active phases reveal a gradual decrease in θ_{O-Ni-O} for di-μ-oxo bridged $Ni^{IV}-Ni^{IV}$ and an increase for di-μ-oxo bridged $Ni^{II}-Fe^{III}$ upon successive Fe incorporation (Fig. 5D). The Fe-dependent change in θ_{O-Ni-O} values for both structural motifs implies that the increased trigonal distortion in di-μ-oxo $Ni^{II}-Fe^{III}$ motifs exacerbates the distortion of neighbouring di-μ-oxo $Ni^{IV}-Ni^{IV}$ motifs.

We propose that the inverted effect that Fe has on the trigonal distortion of the oxidized and reduced phases introduces geometric strain that underlies both the anodic shift of the pre-catalytic redox process and the changes in electrocatalytic performance for $Fe_{100-y}Ni_yO_x$. The epitaxial growth of the perovskite $LaNiO_3$ on selected substrates was recently shown to improve electrocatalytic OER performance by introduction of compressive strain into the crystalline lattice.[35] The strain was shown to induce splitting of the e_g orbitals of Ni ions, improving catalytic performance by altering both the energy and population of d-orbitals. The standard potential for a redox reaction is directly related to the change in Gibbs energy for that reaction; the synchronized, linear anodic shift that is observed for $E_{p,a}$ and $E_{p,c}$ therefore signifies an increased Gibbs energy requirement to drive the oxidation of Ni^{II} to Ni^{IV}. We assign $E_{p,a}$ and $E_{p,c}$ to the redox activity of di-μ-oxo Ni–Ni motifs and attribute the *ca.* 2 mV%$_{Fe}{}^{-1}$ shift in $E_{p,a}$ and $E_{p,c}$ to the increase in magnitude of the trigonal distortion in di-μ-oxo $Ni^{IV}-Ni^{IV}$ motifs induced by neighbouring di-μ-oxo Fe–Ni motifs, which would effectively decrease the thermodynamic stability of the oxidized species. We attribute the abrupt decrease in E_{OER} and change in Tafel slope upon incorporation of Fe into the material to OER catalysis at di-μ-oxo Ni–Fe motifs. Spectroelectrochemical measurements identified two distinct changes in optical properties in Fe-containing compositions but only a single change in 100% Ni. Electrochromism has been

This journal is © The Royal Society of Chemistry 2018

Energy Environ. Sci., 2018, **11**, 2476–2485 | **2483**

reported at *ca.* −0.5 V *vs.* SCE for the transition between $Fe^{II}(OH)_2$ and $Fe^{III}OOH$;[36,37] the observation of exclusively Fe^{III} in the materials here, and the voltage at which the transition occurs, therefore leads us to assign the second electrochromic transition to the oxidation of di-μ-oxo bridged Ni^{II}–Fe^{III} motifs to di-μ-oxo bridged Ni^{IV}–Fe^{III}. We conclude that the oxidation of nickel ions in di-μ-oxo bridged Ni^{II}–Fe^{III} motifs is the relevant process for electrocatalytic OER. Following reports of binuclear reactions in disordered cobalt oxides,[38] we cannot rule out the possibility of a cooperative binuclear reaction. This assertion is supported by observation of static E_{OER} values and Tafel slopes for all Fe-containing compositions in the series, and by the spectroelectrochemical behaviour. The failure to observe a plateau in $\Delta A_{430\,nm}$ as catalytic OER currents increase is also indicative of the minor equilibrium reaction necessary for the observed exponential relationship between current and voltage. Further, a comparison of $\log(d\Delta A_{430\,nm}/dE)$ to $\log(j)$ for the steady state electrochemical data reveals that the second electrochromic process tracks the electrocatalytic currents from *ca.* 60 mV above E_{OER} to the highest voltages examined (Fig. S9, ESI†); resolution of changes closer to E_{OER} are impeded by tailing of optical changes from the initial electrochromic transition. Finally, we propose that the decreased overall strain in the reduced samples may underlie the tendency for nickel hydroxide to scavenge Fe^{III} impurities from solution,[7,8] while the increased strain in the oxidized phase may be related to the reported loss of Fe^{III} from Fe–Ni (oxy)hydroxide films during OER catalysis.[39]

Conclusions

A series of disordered metal oxide films based on the formula $Fe_{100-y}Ni_yO_x$ were prepared and characterized by X-ray absorption spectroscopy and spectroelectrochemistry. Systematic structural analysis by X-ray absorption fine-structure spectroscopy identified four distinct structural features that are dependent on both voltage and composition. The structural data indicate a trigonal distortion in both the oxidized and reduced forms of 100% Ni, with O–Ni–O angles of *ca.* 82°. Composition- and voltage-dependent trends in the structural data indicate that incorporation of Fe^{III} into the material has inverted effects on this trigonal distortion in the oxidized and reduced phases: Fe^{III} decreases the geometric strain in the reduced phase but exacerbates it in the oxidized phase. We conclude that this inverted effect on the trigonal distortion introduces an energy penalty for oxidation of Ni^{II} to Ni^{IV}, yielding the observed 2 mV%$_{Fe}^{-1}$ shift observed for $E_{p,a}$ and $E_{p,c}$. We report a secondary change in optical absorbance at *ca.* 1.5 V for Fe-containing compositions which we assign to oxidation of di-μ-oxo Ni^{II}–Fe^{III} sites. We attribute the abrupt improvement in OER performance upon Fe incorporation to the geometric strain present in di-μ-oxo Ni^{IV}–Fe^{III} sites. The introduction of geometric distortions by incorporation of redox inactive sites may prove to be an effective electrocatalyst design strategy.

Conflicts of interest

There are no conflicts to declare.

Notes and references

1 T. R. Cook, D. K. Dogutan, S. Y. Reece, Y. Surendranath, T. S. Teets and D. G. Nocera, *Chem. Rev.*, 2010, **110**, 6474–6502.

2 M. G. Walter, E. L. Warren, J. R. McKone, S. W. Boettcher, Q. Mi, E. A. Santori and N. S. Lewis, *Chem. Rev.*, 2010, **110**, 6446–6473.

3 J. Suntivich, K. J. May, H. A. Gasteiger, J. B. Goodenough and Y. Shao-Horn, *Science*, 2011, **334**, 1383–1385.

4 J. F. Bringley, B. A. Scott, S. J. La Placa, R. F. Boehme, T. M. Shaw, M. W. McElfresh, S. S. Trail and D. E. Cox, *Nature*, 1990, **347**, 263–265.

5 P. Rüetschi and P. Delahay, *J. Chem. Phys.*, 1955, **23**, 556–560.

6 L. C. Seitz, C. F. Dickens, K. Nishio, Y. Hikita, J. Montoya, A. Doyle, C. Kirk, A. Vojvodic, H. Y. Hwang, J. K. Nørskov and T. F. Jaramillo, *Science*, 2016, **353**, 1011–1014.

7 D. A. Corrigan, *J. Electrochem. Soc.*, 1987, **134**, 377–384.

8 L. Trotochaud, S. L. Young, J. K. Ranney and S. W. Boettcher, *J. Am. Chem. Soc.*, 2014, **136**, 6744–6753.

9 M. W. Louie and A. T. Bell, *J. Am. Chem. Soc.*, 2013, **135**, 12329–12337.

10 S.-H. Ye, Z.-X. Shi, J.-X. Feng, Y.-X. Tong and G.-R. Li, *Angew. Chem., Int. Ed.*, 2018, **57**, 2672–2676.

11 M. S. Burke, M. G. Kast, L. Trotochaud, A. M. Smith and S. W. Boettcher, *J. Am. Chem. Soc.*, 2015, **137**, 3638–3648.

12 M. Görlin, P. Chernev, F. J. Araujo, T. Reier, S. Dresp, B. Paul, R. Krähnert, H. Dau and P. Strasser, *J. Am. Chem. Soc.*, 2016, **138**, 5603–5614.

13 D. Friebel, M. W. Louie, M. Bajdich, K. E. Sanwald, Y. Cai, A. M. Wise, M.-J. Cheng, D. Sokaras, T.-C. Weng, R. Alonso-Mori, R. C. Davis, J. R. Bargar, J. K. Nørskov, A. Nilsson and A. T. Bell, *J. Am. Chem. Soc.*, 2015, **137**, 1305–1313.

14 J. Y. C. Chen, L. Dang, H. Liang, W. Bi, J. B. Gerken, S. Jin, E. E. Alp and S. S. Stahl, *J. Am. Chem. Soc.*, 2015, **137**, 15090–15093.

15 Z. K. Goldsmith, A. K. Harshan, J. B. Gerken, M. Vörös, G. Galli, S. S. Stahl and S. Hammes-Schiffer, *Proc. Natl. Acad. Sci. U. S. A.*, 2017, **114**, 3050–3055.

16 B. M. Hunter, N. B. Thompson, A. M. Müller, G. R. Rossman, M. G. Hill, J. R. Winkler and H. B. Gray, *Joule*, 2018, **2**, 747–763.

17 N. Li, D. K. Bediako, R. G. Hadt, D. Hayes, T. J. Kempa, F. von Cube, D. C. Bell, L. X. Chen and D. G. Nocera, *Proc. Natl. Acad. Sci. U. S. A.*, 2017, **114**, 1486–1491.

2484 | *Energy Environ. Sci.*, 2018, **11**, 2476–2485

This journal is © The Royal Society of Chemistry 2018

18 R. D. L. Smith, M. S. Prevot, R. D. Fagan, Z. Zhang, P. A. Sedach, M. K. J. Siu, S. Trudel and C. P. Berlinguette, *Science*, 2013, **340**, 60–63.

19 R. D. L. Smith, M. S. Prevot, R. D. Fagan, S. Trudel and C. P. Berlinguette, *J. Am. Chem. Soc.*, 2013, **135**, 11580–11586.

20 R. D. L. Smith, C. Pasquini, S. Loos, P. Chernev, K. Klingan, P. Kubella, M. R. Mohammadi, D. Gonzalez-Flores and H. Dau, *Nat. Commun.*, 2017, **8**, 2022.

21 A. L. Ankudinov, B. Ravel, J. J. Rehr and S. D. Conradson, *Phys. Rev. B*, 1998, **58**, 7565–7576.

22 M. Risch, K. Klingan, J. Heidkamp, D. Ehrenberg, P. Chernev, I. Zaharieva and H. Dau, *Chem. Commun.*, 2011, **47**, 11912–11914.

23 D. K. Bediako, B. Lassalle-Kaiser, Y. Surendranath, J. Yano, V. K. Yachandra and D. G. Nocera, *J. Am. Chem. Soc.*, 2012, **134**, 6801–6809.

24 R. D. L. Smith and C. P. Berlinguette, *J. Am. Chem. Soc.*, 2016, **138**, 1561–1567.

25 R. D. L. Smith, R. S. Sherbo, K. E. Dettelbach and C. P. Berlinguette, *Chem. Mater.*, 2016, **28**, 5635–5642.

26 D. A. Corrigan and R. M. Bendert, *J. Electrochem. Soc.*, 1989, **136**, 723–728.

27 D. A. Corrigan and S. L. Knight, *J. Electrochem. Soc.*, 1989, **136**, 613–619.

28 I. Zaharieva, P. Chernev, M. Risch, K. Klingan, M. Kohlhoff, A. Fischer and H. Dau, *Energy Environ. Sci.*, 2012, **5**, 7081–7089.

29 M. Risch, F. Ringleb, M. Kohlhoff, P. Bogdanoff, P. Chernev, I. Zaharieva and H. Dau, *Energy Environ. Sci.*, 2015, **8**, 661–674.

30 A. N. Mansour and C. A. Melendres, *J. Phys. Chem. A*, 1998, **102**, 65–81.

31 H. Dau, P. Liebisch and M. Haumann, *Anal. Bioanal. Chem.*, 2003, **376**, 562–583.

32 M. Risch, V. Khare, I. Zaharieva, L. Gerencser, P. Chernev and H. Dau, *J. Am. Chem. Soc.*, 2009, **131**, 6936–6937.

33 M. W. Kanan, J. Yano, Y. Surendranath, M. Dincă, V. K. Yachandra and D. G. Nocera, *J. Am. Chem. Soc.*, 2010, **132**, 13692–13701.

34 D. S. Hall, D. J. Lockwood, C. Bock and B. R. MacDougall, *Proc. R. Soc. A*, 2014, **471**, 20140792.

35 J. R. Petrie, V. R. Cooper, J. W. Freeland, T. L. Meyer, Z. Zhang, D. A. Lutterman and H. N. Lee, *J. Am. Chem. Soc.*, 2016, **138**, 2488–2491.

36 T. Maruyama and T. Kanagawa, *J. Electrochem. Soc.*, 1996, **143**, 1675–1677.

37 B. Orel, M. Macek, F. Svegl and K. Kalcher, *Thin Solid Films*, 1994, **246**, 131–142.

38 C. N. Brodsky, R. G. Hadt, D. Hayes, B. J. Reinhart, N. Li, L. X. Chen and D. G. Nocera, *Proc. Natl. Acad. Sci. U. S. A.*, 2017, **114**, 3855–3860.

39 F. D. Speck, K. E. Dettelbach, R. S. Sherbo, D. A. Salvatore, A. Huang and C. P. Berlinguette, *Chem*, 2017, **2**, 590–597.

This journal is © The Royal Society of Chemistry 2018

Energy Environ. Sci., 2018, **11**, 2476–2485 | **2485**